Journal of Pharmaceutical Sciences 114 (2025) 507–519

Contents lists available at ScienceDirect

Journal of Pharmaceutical Sciences

journal homepage: www.jpharmsci.org

Pharmaceutics, Drug Delivery and Pharmaceutical Technology

Structure, morphology and surface properties of α-lactose monohydrate in relation to its powder properties

Thai T.H. Nguyen[a,1], Cai Y. Ma[a], Ioanna D. Styliari[b], Parmesh Gajjar[c,d,2], Robert B. Hammond[a], Philip J. Withers[c,d], Darragh Murnane[b], Kevin J. Roberts[a,*]

[a] Centre for the Digital Design of Drug Products, School of Chemical and Process Engineering, Institute of Process, Research & Development, University of Leeds, Leeds LS2 9JT, UK
[b] School of Life and Medical Sciences, University of Hertfordshire, Hertfordshire AL10 9AB, UK
[c] Henry Moseley X-ray Imaging Facility, Department of Materials, The University of Manchester, Manchester M13 9PL, UK
[d] Henry Royce Institute for Advanced Materials, Department of Materials, The University of Manchester, Manchester M13 9PL, UK

ARTICLE INFO

Article history:
Received 13 August 2024
Revised 17 October 2024
Accepted 17 October 2024
Available online 29 October 2024

Keywords:
A-lactose monohydrate
Morphological characterisation
Inhalation powdered drug formulations
Synthons and intermolecular interactions
Surface energy
Surface physical chemical properties
X-ray computed tomography
Mechanical properties

ABSTRACT

The particulate properties of α-lactose monohydrate (αLMH), an excipient and carrier for pharmaceuticals, is important for the design, formulation and performance of a wide range of drug products. Here an integrated multi-scale workflow provides a detailed molecular and inter-molecular (synthonic) analysis of its crystal morphology, surface chemistry and surface energy. Predicted morphologies are validated in 3D through X-ray diffraction (XCT) contrast tomography. Interestingly, from aqueous solution the fastest growth is found to lie along the b-axis, i.e. the longest unit cell dimension of the αLMH crystal structure reflecting the greater opportunities for solvation on the prism compared to the capping faces leading to the former's slower relative growth rates. The tomahawk morphology reflects the presence of β-lactose which asymmetrically binds to the capping surfaces creating a polar morphology. The crystal lattice energy is dominated by van der Waals interactions (between lactose molecules) with electrostatic interactions contributing the remainder. Predicted total surface energies are in good agreement with those measured at high surface coverage by inverse gas chromatography, albeit their dispersive contributions are found to be higher than those measured. The calculated surface energies of crystal habit surfaces are not found to be significantly different between different crystal surfaces, consistent with αLMH's known homogeneous binding to drug molecules when formulated. Surface energies for different morphologies reveals that crystals with the elongated crystal morphologies have lower surface energies compared to those with a triangular or tomahawk morphologies, correlating well with literature data that the surface energies of the lactose carriers are inversely proportional to their aerosol dispersion performance.

Introduction

The simple milk sugar lactose ($C_{12}H_{22}O_{11}$) is commonly used as a stabiliser and carrier in both the food and pharmaceutical sectors. In the latter case, lactose acts as a bulking excipient in tablets, or a carrier for active pharmaceutical ingredients (API) in inhaled formulations. Understanding and characterising the bulk and surface structures of lactose are important in formulation notably for ensuring its powder flow, agglomeration, content uniformity, compaction properties and formation of interacting mixtures[1] with micronized drug particles for inhalation. Lactose is a disaccharide consisting of galactose and glucose moieties both of which are in their pyranose forms and which are interconnected through a covalently-bonded β 1-4 glycosidic linkage (Fig. 1)[2] which can exist in two anomeric forms: α-lactose and β-lactose. The two anomers can interconvert $\alpha \leftrightarrow \beta$ via a solution-mediated mutarotation process characterised by a phase equilibrium ratio β to α that varies of between 1.25 - 1.64, depending on the temperature and solution concentration.[3]

Lactose crystallisation can result in four known solid forms: anhydrous β-lactose, α-lactose with hygroscopic and stable anhydrous forms, and α-lactose monohydrate (αLMH) .[4] Their crystal structures have all been reported in literature.[5,6] The methods for preparing

Dedicated to the life and research works of Professor Lynne S Taylor

* Corresponding author.
E-mail address: k.j.roberts@leeds.ac.uk (K.J. Roberts).
[1] School of Computing, University of Leeds, Woodhouse Lane, Leeds, LS2 9JT, UK
[2] InformiX Pharma Limited, Unit 6 Church Farm, Church Road, Bury St. Edmunds, IP29 5AX, UK

https://doi.org/10.1016/j.xphs.2024.10.031

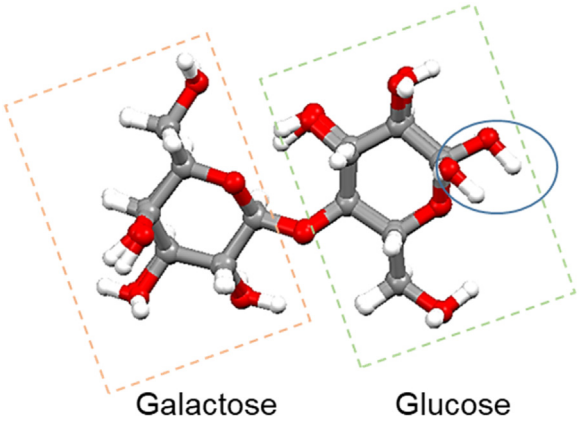

Fig. 1. Overlay of the optimised molecular structures of αL and βL showing combination of the galactose and glucose moieties. Their main difference is the orientation of a hydroxyl group in the glucose moiety (circled in blue). (For interpretation of the references to color in this figure legend, the reader is referred to the web version of this article.)

various structural modifications of αLMH are reported in **Table S1** (Supporting Information (SI)). It is important to note that αLMH crystals mostly do not grow from a pure environment, i.e. their growth environment always contains some β-lactose.

The crystalline solid form of αLMH is one of the most widely used excipients for pharmaceutical applications,[7] leading to an extensive research examining its crystallization[4,8–11] and agglomerative/adhesive behaviors.[12–18] Previous studies have shown that αLMH crystal morphology depends on the crystallisation conditions[11,12] and β-lactose fraction present in the solution.[9] β-lactose stereochemically selectively blocks the growth of the polar (010) and (0−10) crystal faces, resulting in preferential adsorption of β-lactose on the latter face. This leads to preferential growth of the (010) face, giving rise to the characteristic polar tomahawk morphology of αLMH crystals.[8,19]

For orally-administered formulations such as tablets, αLMH excipients play a significant role in formulation stability and bioavailability.[20] In the case of inhalation formulations, low-dose APIs are currently formulated with coarse "carrier" αLMH particles, that function as formulation diluents, but also act to improve the flow, dose uniformity, dispersion, and aerosolization of micronized ($< 5\ \mu$m)[21] drug particles.[13,15,22,23] Studies on dry powder inhalation formulations have shown that for particles that have similar size, surface area and density, the aerosol dispersion performance is inversely proportional to the surface energies of lactose carriers.[24–26] Crystallization of αLMH with different morphologies correlated with the increase of the surface energy of the carrier particles, and increasing difficulty for the drug to detach from the carrier and be aerosolized.[26,27] The increase of either the surface smoothness or the elongation ratio of lactose crystals would increase the potentially respirable fraction of the APIs within dry powder inhalation formulations.[28] The particle size range and deviation from αLMH's tomahawk shape are key aspects determining the surface area of individual crystal facets and consequently the adhesive/cohesive surface energy that underpins API content uniformity and aerosolization efficiency.[29–31]

Up to now, prediction of formulation efficiency has relied on the experimental determination of the inter-particle forces using techniques such as inverse gas chromatography (IGC) and atomic force microscopy.[30] Inter-molecular simulations offer an alternative approach for prediction and exploration of inter-particulate surface interactions in formulation science. Synthons, defined as the interaction between paired molecules arising from hydrogen bonding, van der Waals and coulombic interactions, are also dominating forces of inter-particulate interactions. Synthonic engineering techniques have been utilised to predict the crystal surface-terminated intermolecular interactions (extrinsic synthons) (see for example,[32,33]), crystal morphology and surface chemistry, and also the mediation of the crystal growth process by additives or impurities or hydration[24,25,33–40] as well as for the generation of interaction energy maps.[36,41–44] A digital workflow has been developed for predicting the physicochemical properties of relevance to inhaled formulations based on the synthonic features of API crystal morphology and surface chemistry.[24]

The crystal morphology of αLMH has been previously reported,[45–47] and used to perform molecular simulations of the cohesive/adhesive force balance between αLMH and inhalation APIs.[25] A new approach encompassing molecular-scale modelling and XCT[48] techniques has been developed in order to both predict and quantify the crystal facet interactions at the particle−particle level within a powder bed.[49,50] Furthermore, a recent study[44] has simulated and examined the interparticle interactions within terbutaline sulfate and αLMH blends, which were linked with product performance through the assessment of the predicted adhesive and cohesive energies and their balances within the blends.

Building upon the above perspective, this paper seeks to provide a more rigorous and molecular-scale understanding of crystal morphology and surface properties of αLMH using inter-molecular (synthonic) modelling approaches.[51] More generally, this study also aims to demonstrate the utility of a digital design methodology, based upon crystallographic information, for the design of formulations needed for the delivery of inhaled drugs. The techniques have been employed to predict material-specific surface properties related to particle cohesion and agglomeration behaviour. In this way the aim has been to develop a pathway and workflow to reduce the amount of laboratory-based pre-formulation assessment needed for drug product development.

Materials and methods

A four-stage workflow, summarised in Fig. 2, highlights the interrelationship between the molecular, solid-state, surface and particle properties of αLMH used. The workflow illustrates the pathway from the material's core molecular chemistry to the solid-state structure (intrinsic intermolecular interactions) and then to the individual surface structure properties (extrinsic intermolecular interactions) and their interaction to predict the overall particle properties.

Materials

The crystallographic data of αLMH (refcode: LACTOS11)[6] was accessed from the CCDC; its structure was determined at low temperature with a reasonably low R factor of 3.32 %. αLMH ($C_{12}H_{22}O_{11}.H_2O$) revealing that it crystallised in a polar bimolecular monoclinic structure with space group $P2_1$, cell parameters a = 4.78 Å, b = 21.54 Å, c = 7.76 Å, β = 105.91° and unit cell volume 768.8 Å^3. β-lactose (refcode: BLACTO02)[5] was also found to crystallise in a polar monoclinic structure with space group $P2_1$, cell parameters a = 4.93 Å, b = 13.27 Å, c = 10.78 Å, β = 91.55° and unit cell volume 705.3 Å^3.

αLMH, BioXtra, ≥ 99 % total lactose basis (GC) was purchased from Sigma Aldrich and used as supplied. For IGC measurements, inhalation grade α-lactose monohydrate, namely Lactohale 100 (sieved, batch 101NN16), was kindly supplied by DFE Pharma (GmbH).

Computational studies

Molecular properties

The molecular surface areas were calculated using the Connolly surface tool within Material Studio,[52] using a grid interval of 0.25 Å and a probe radius of 1 Å. The void fraction was calculated using Mercury 4.0[53] based on 0.2 for both probe radius and grid spacing.[54] The dipole moment of the molecule was calculated using the density

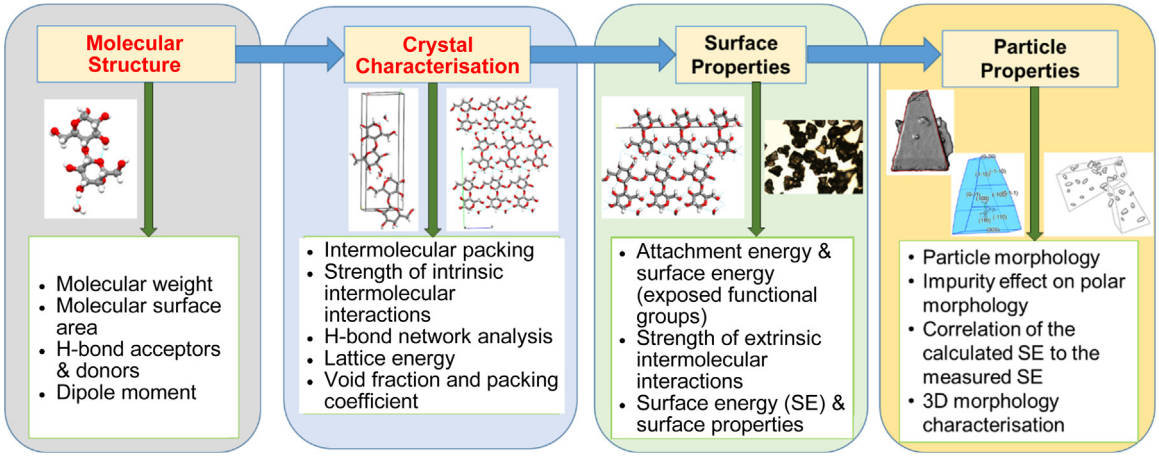

Fig. 2. Predictive workflow for inhalation drug formulation highlighting the 4-stage pathway from the molecular state through solid-state and surface properties to the blended powder.

functional theory method with exchange-correlation B3LYP (Becke 3-parameter; Lee, Yang, Parr)[55,56] functional and basic set TZVP using the CRYSTAL program.[57]

Bulk properties

The computational analysis was carried out utilizing Mercury,[53] HABIT98[58] and Materials Studio.[52] Partial atomic-charges were calculated using the semi-empirical quantum mechanics program MOPAC[59] utilizing the Austin Model 1 (AM1) approach with 1 self-consistent field calculation. The strength and nature of the fully bound (intrinsic) intermolecular synthons and the lattice energy (E_{cr}), were calculated using HABIT98,[58] with the Momany intermolecular forcefield.[60] An intermolecular summation radius of between 10 and 50 Å was used to ensure lattice energy convergence.

Surface properties

The expected crystal habit surface planes {*hkl*} were calculated using the BFDH method.[61–63] The unsatisfied or broken (extrinsic) intermolecular synthons associated with surface termination were calculated by partitioning the bulk intrinsic synthons between those contributing to the surface slices (intrinsic) E_{sl}^{hkl} and their attachment (extrinsic) E_{att}^{hkl} energies, respectively for each potential crystal surface plane form {*hkl*} as given in the following equation.

$$E_{cr} = E_{att}^{hkl} + E_{sl}^{hkl} \quad (1)$$

The anisotropy factor ξ_{hkl}, reflecting the degree of synthon saturation of a molecule when it is surface terminated, i.e. fraction of the intermolecular interactions that have been unbroken, was calculated using the following equation.

$$\xi_{hkl} = \frac{E_{sl}}{E_{cr}} \quad (2)$$

Molecules residing within the bulk of a crystal lattice are subjected to three dimensional packing forces exerted by the surrounding molecules. However, for molecules at a crystal surface in equilibrium with a vacuum, these forces become anisotropic causing these surface molecules to have a different intermolecular arrangement when compared to that in the bulk. The surface energy can thus be defined as the additional energy possessed by the surface molecules in equilibrium with a vacuum compared to the corresponding molecules in the bulk.[64–66] The different arrangement of molecules on different habit faces thus results in different surface chemistry and hence surface energy. The surface energy (SE) was calculated directly from the predicted attachment energy[64–67] using the following equation

$$\gamma = \gamma_{disp} + \gamma_{polar} = \frac{Z\ d_{hkl}}{2\ N_A\ V}\ (E_{att(vdw)} + E_{att(es)}) = \frac{Z\ d_{hkl}\ |E_{att}|}{2\ N_A\ V} \quad (3)$$

where Z is the number of molecules per unit cell, d_{hkl} is the thickness of the growth step layer, N_A is Avogadro's constant, and V is the unit cell volume. The predicted dispersive (γ_{disp}) and electrostatic (γ_{es}) components of surface energy were calculated from the attachment energy (E_{att}) contributions from the van der Waals ($E_{att\ (vdw)}$) and electrostatic ($E_{att(es)}$) components of the intermolecular interactions.

The interaction energies for a β-lactose probe molecule onto the crystal habit surfaces (020) and (0-20) of αLMH were predicted using the SystSearch program.[25] This program performed a grid-based (systematic) search of probe/surface intermolecular interactions through generation of a molecular model of a specific crystal habit surface with well-defined surface terminations to retain complete molecules in the host surface. In this approach, a probe molecule was used to explore the energy landscape as it interacts with the surface. The probe molecule, treated as a rigid body, was placed point by point within the built grid in turn with a step size of 1 Å and was orientated, sequentially, into one of a number of specified orientations. The intermolecular energy of the probe/surface combination was calculated using a pairwise atom-atom interaction energy with a probe molecule having a cut-off radius of 25 Å. From these observations, the interaction energy of a probe molecule on a particular habit surface plane was calculated for each grid point using an experientially derived empirical Dreiding II atomic force field[68] together with partial charges calculated using the MOPAC method[59] for electrostatic contributions. The generated energy distribution of favourable binding sites and the minimum interaction energy were calculated based upon the most likely binding position of probe molecule on the surface.[25,36,43,44]

Particle properties

The attachment energies were taken as a measure of the relative growth rates of the crystal habit surfaces. These were normalised and used to construct a 3D Wulff plot[69] using the graphical routines within Mercury[53] and, through this, provide a 3D representation of the predicted crystal morphology. Note that the predicted morphology may be different from the experimentally observed one due to the different conditions used for prediction (vacuum) and experiment (solvent).

The overall particle surface energy ($\gamma_{particle}$)[66] was calculated on the basis of the crystal surface areas as predicted from the morphological simulation. From this, a surface area-weighted whole crystal surface energy was calculated via Eq. (4) after,[66]

$$\gamma_{particle} = \sum_{i=1}^{n} \gamma_i^{hkl} A_i^{hkl} M_i^{hkl} \quad (4)$$

where n is the number of forms (family of crystallographically equivalent faces), γ_i^{hkl} is the surface energy of individual crystal surfaces, A_i^{hkl} is the fractional surface area of the habit face and M_i^{hkl} is the multiplicity of the crystallographically equivalent habit faces.

The effect of crystal habit variation on the base-line predicted crystal morphology can be achieved by modifying the centre-to-face distances in the Wulff plot. Through this, the crystal morphology is modified with the surface areas of the crystal habit faces being adjusted to match those of the observed crystal morphologies for the crystals prepared under different crystallisation conditions. Based on these habit faces, their surface energies are calculated and compared with experimentally measured ones.

Experimental studies

Crystal growth

αLMH single crystals were prepared by crystallisation from solution by adding 47.7 g LMH to 100 g water (% by mass). This solution was then heated to 70 °C and stirred for 30 min to ensure complete solute dissolution, then rapidly cooled to 25 °C and left until crystallization occurred. An Olympus BX51 microscope, with a UMPlanFl 10×/0.30 objective was used to characterize the size and shape of the resultant crystals.

Surface energy measurements by inverse gas chromatography

Specific surface area and surface energy (SE) analyses were conducted using an Inverse Gas Chromatography Surface Energy Analyser (IGC-SEA, Surface Measurement Systems Ltd, UK). Approximately 1.5 g of lactose powders were packed into a silanised glass IGC column with an internal diameter of 4 mm. Prior to any measurements, the loaded column was conditioned using helium carrier gas at 10 scc/min for 2 h at 30 °C and 0 % RH. Methane gas was injected at the start and the end of the experiments for the dead volume calculation. Specific surface areas were calculated via the Brunauer–Emmett–Teller theory, based on the n-octane adsorption isotherm data.[25] For the surface energy, the columns were equilibrated as above. Non-polar probes (n-decane, n-nonane and n-octane) and polar probes (chloroform, toluene, ethyl acetate) were injected in the column at a range of surface coverages (n/nm). Following a previously reported analysis method,[21,70] the dispersive (γ_d, non-polar) and acid-base (γ_{ab}, polar) components of the surface energy were calculated using the Dorris-Gray method[71] and the Peak centre of mass parameter.[72] All the measurements were made in triplicate in a single packed column. Note that other probes such as undecane and dodecane could be used in further work to verify the findings in this study with three non-polar and three polar probes.

X-ray tomographic characterisation

A single crystal of αLMH was glued to the end of a toothpick[73] and scanned in an Zeiss Xradia 520 Versa X-ray microscope equipped with a LabDCT[74] module (Carl Zeiss Microscopy, California, USA). An absorption contrast scan was acquired with 3000 projections, with each projection having an exposure time of 1.5 s each. The source voltage was 50 kV with the current being 80 μA. The raw projections were reconstructed using the XMReconstructor software within the X-ray Microscope system to form a 3D virtual volume, which was visualised using Dragonfly Pro 4.1 (Object Research Systems, Canada).

Table 1
Summary of some key molecular and crystallographic descriptors for αLMH.

Property	Property value
Molecular Mass	360.31 g/mol
Atom count	48
Molecular dimension (x,y,z)	5.13, 11.95, 7.21
Molecular surface area (Connolly surface)	314.30 Å^2
Molecular volume	308.54 Å^3
Void fraction	0.228
Packing coefficient	0.732
Number of Hydrogen bond donors	
• Lactose	8
• Water	2
Number of Hydrogen bond acceptors	
• Lactose	9
• Water	1
Dipole moment (x,y,z) (Debye, D)	1.81, 7.63, −1.26
Total dipole moment	7.94

The single lactose crystal was segmented from the toothpick, and then viewed from different crystallographic directions. The angles between the crystal's facets were measured using the opensource vector graphics software Inkscape (version 0.92).[75]

Results and discussion

Molecular properties

The molecular and crystallographic descriptors for αLMH summarised in Table 1 provide an indication of its molecular and physicochemical properties. The data reveal αLMH to be of medium molecular weight (360.31 g mol^{-1}) compared to representative pharmaceuticals of < 500 g mol^{-1} [54] which have a median of around 350 g mol^{-1} [76]. The structure can be seen to have a relatively large number of intermolecular hydrogen bonding options associated with eight donors from the hydroxyl and water groups with eleven potential acceptors from the hydroxyl and water groups. From a molecular polarizability perspective, the αLMH molecule was found to be more polar in the y direction than in the x and z directions with their values being 7.63 D, 1.81 D and −1.26 D, respectively. The atomic charge distribution calculated on the basis of the isolated molecule is listed in Table S2 (SI) with their atom numbering shown in Fig. 3(a). A 2D view of the molecular structure of αLMH is given in Fig. 3(b) highlighting the galactose and glucose moieties, and the four hydroxyls groups from each molecule in the unit cell.

Solid-state properties

Bulk crystal chemistry and local inter-molecular co-ordination

The intermolecular packing and bulk crystal chemistry of αLMH is highlighted in Fig. 3(b–d). Overall, its crystal structure is comparatively simple with just two molecules each of lactose and its hydration water within the unit cell. These are related by a 2 fold screw axis with the oriented long axis of the molecules being aligned approximately parallel to the b crystallographic axis which, as a result, forms the longest axis of the unit cell. The lack of any mirror or inversion symmetry elements gives rise to a polar structure notably associated with all the glucose moieties pointing in one direction (see Fig. 3(b)) of the crystallographic b-axis with the galactose moieties aligned in the opposite direction. Fig. 4 highlights the packing diagram of αLMH structure viewed along the a and c axes, showing the inter-molecular hydrogen bonding network of four lactose molecules co-ordinating to a single water molecule. It also shows the stacking formation of the lactose molecules and hydrogen bonding linking molecules of lactose and water within the crystal structure. The low crystal symmetry and hence simplicity of the crystal

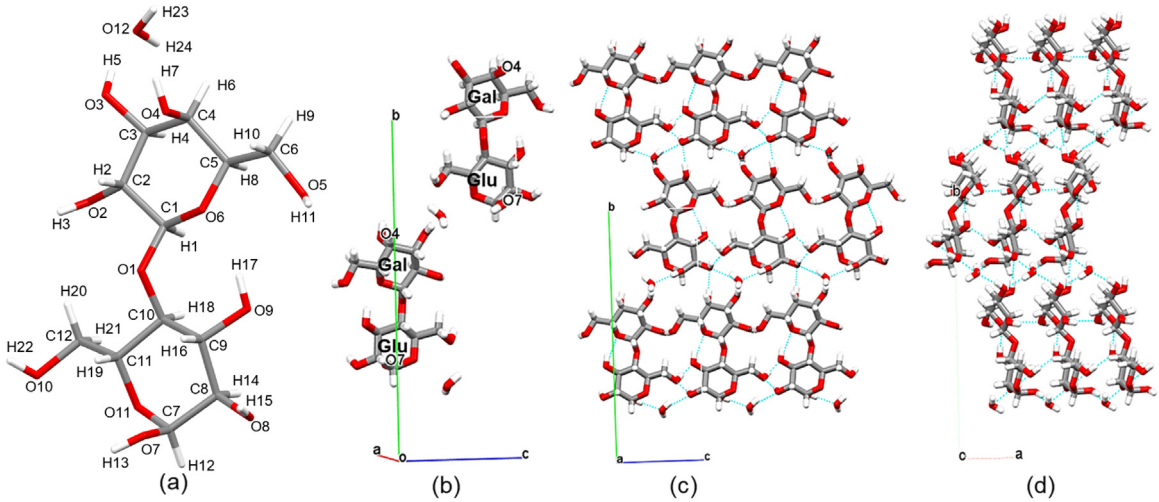

Fig. 3. Intermolecular packing diagrams highlighting the crystal structure (CSD reference LACTOS11) and crystal chemistry of αLMH : (a) Atom numbers with partial atomic charges (Table S2) calculated for an isolated molecule using MOPAC; (b) Unit cell geometry illustrating the quite simple structural arrangement of the two pairs of lactose and water molecules which are interrelated by the 2_1 screw axis; (c and d) Intermolecular packing normal to the a and c axes, respectively showing the interaction of lactose molecules with the water molecules arranged in channels parallel to the c and a axis. The hydrogen bonds between a water molecule and 4 lactose molecules also forms a pocket of lactose molecules within which the water molecule can sit.

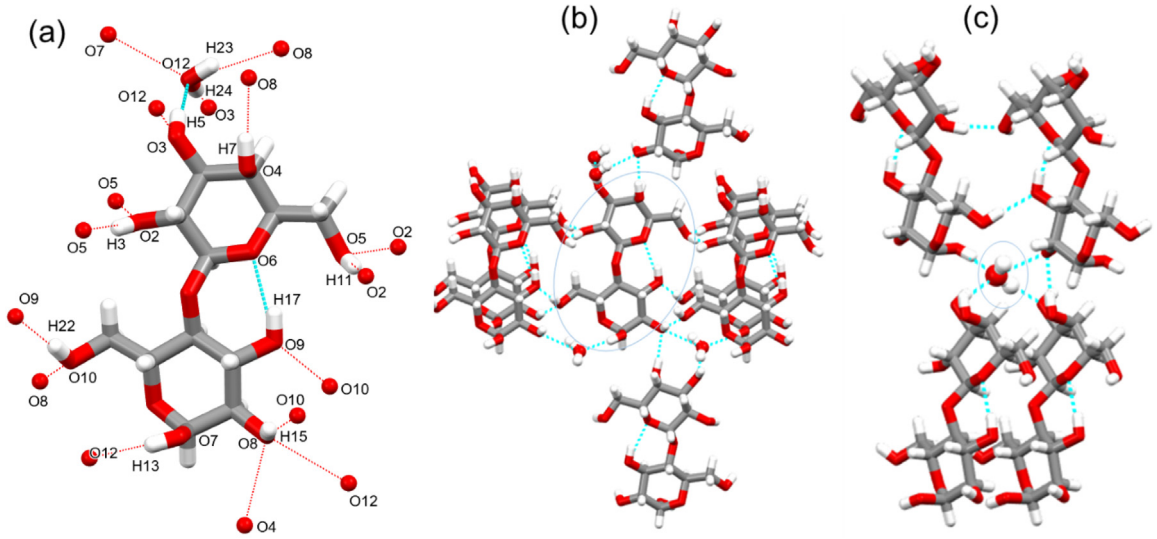

Fig. 4. (a) Hydrogen-bonding network of a αLMH molecule; (b) Intermolecular coordination hydrogen-bonding shell for lactose molecule (circled) highlighting 10 H-bonding interactions with 6 lactose molecules and 4 H-bonding interactions with 4 water molecules; (c) Intermolecular coordination hydrogen bonding shell for a water molecule (circled) highlighting four H-bonds formed with 4 lactose molecules.

chemistry gives rise to a layer-like structure normal to the b-axis, suggesting overall a comparative ease of self-assembly in the solid state.

This structure (Fig. 4) is consistent with the observed thermodynamic instability of both the stable and hygroscopic forms of the anhydrous form of alpha lactose under ambient conditions as it is clear from the crystal chemistry that the crystal structures of anhydrous form alpha lactose can readily absorb moisture from the surrounding environment into the pockets formed by the 4 lactose molecules through the channels (Fig. 3(c&d) and Fig. 4(c)). This has been observed in the literature.[77,78] A comparison study of α-form lactose (hydrate and anhydrous) and other forms of lactose including their thermodynamic stability, molecular and crystal characterisation etc. can deepen our understanding of their bulk powder properties and also formulation performance.

Within the αLMH crystal structure, each α-lactose molecule is also involved in an intramolecular hydrogen-bond between O6 and H17 (H-bond length: 2.016 Å) together with 14 intermolecular hydrogen-bonds (Fig. 4(a)), in a local co-ordination involving binding to 6 lactose molecules and 4 water molecules (Fig. 4(b)). In a similar manner, each water molecule binds with 4 lactose molecules (Fig. 4 (c)), thereby forming a pocket in which the water molecule can sit, aligning well with literature,[79] but there are no direct interactions between the water molecules.

Mechanical properties

Examination of the packing structure of the four lactose molecules found that the pockets form channels along the c and a axes (see Fig. 3(c and d)), leading to the water molecules forming molecule chains and sitting in the channels. Overall, the layer-like structure inherent in the αLMH structure is fully consistent with the material's known mechanical properties[80,81] in that the αLMH moieties can slide past each other along the shorter a and c axes on the {010} plane normal to the crystallographic b-axis without significant steric

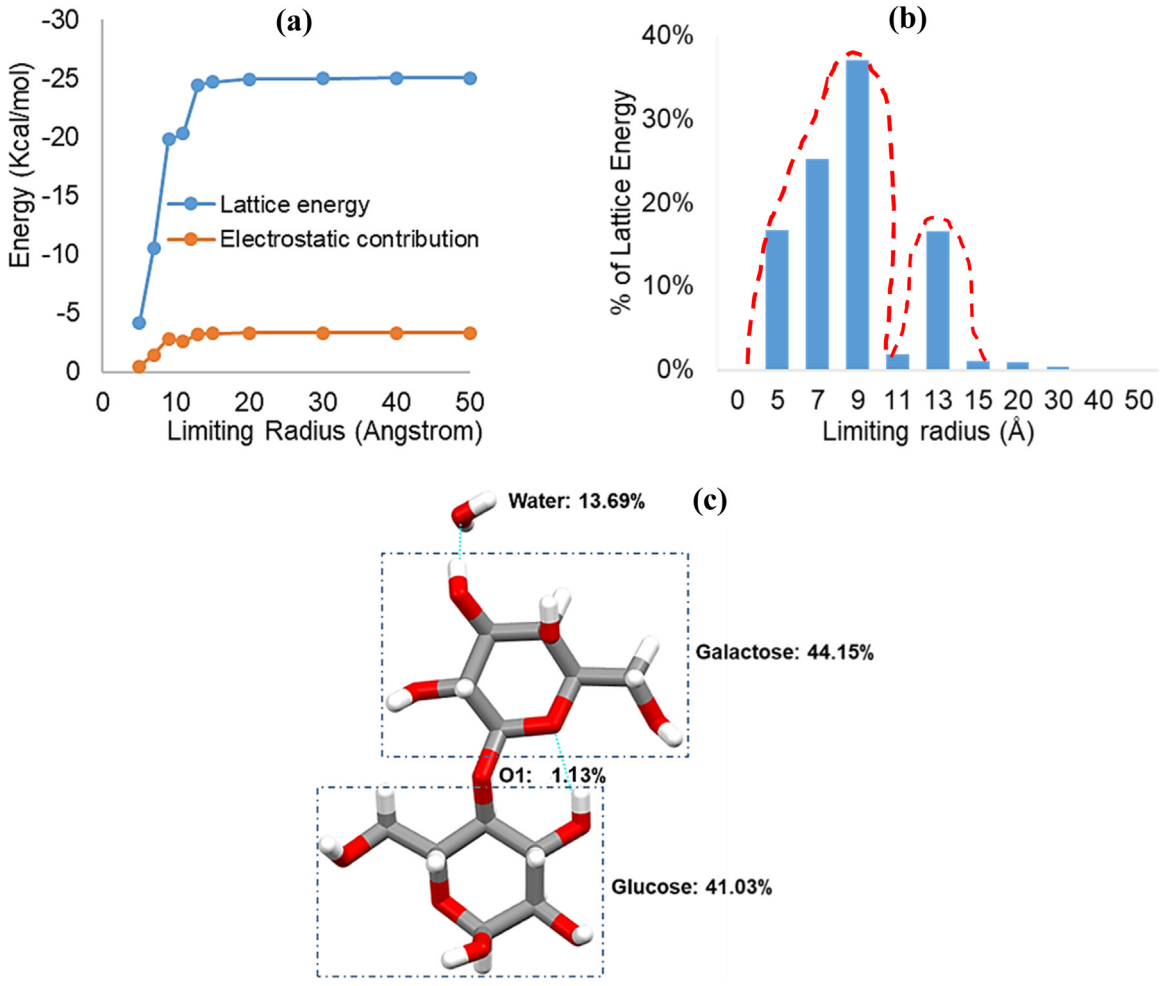

Fig. 5. Lattice energy convergence as a function of limiting radius for αLMH, indicating that (a) interactions above approximately 20 Å are relatively unimportant to the stabilization of the lattice and the contribution of electrostatic interactions to the overall lattice energy is low; (b) radial discretized distribution plots showing the % contribution to the lattice energy as a function of intermolecular summation distance with the dashed lines as guidance to indicate the distributions of the energy contributions from two shells; (c) the percentage % contribution to the lattice energy from the different molecular groups (water, galactose, oxygen (O1) and glucose) of the asymmetric unit showing water contributes 13.69 % to the lattice energy.

hindrance. This would be consistent with the low surface rugosity of the {010} surfaces when compared to the other closer packed planes as shown in Table 3 (column 7). Such a plastic deformation would also suggest (010)[100] and potentially (010)[001] as the likely dislocation slip systems.

Crystal lattice energies

The lattice energy convergence as a function of its intermolecular interaction radius is given in cumulative form in Fig. 5(a). The binding energy increases with more molecules being included in the atom-atom calculation when increasing limiting distance with respect to the origin molecule. The calculated lattice energy of -25.05 kcal mol^{-1}, consistent with that previously reported.[46] The coulombic interactions contribute relatively little to the stability of the αLMH lattice. The lattice energy summation is also given in discretised form in Fig. 5(b) revealing two reasonably well-defined coordination spheres with overall convergence at an intermolecular distance of about 20 Å. Segmentation of the relative contributions of the functional group contributions to the overall lattice energy reveals that the galactose and glucose rings fairly equally dominate the structural stability of αLMH in its solid state with its hydration water only contributing 13.69 % (see Fig. 5). This would be consistent with water representing less than 10% of the total mass within the asymmetric unit.

Intrinsic synthon analysis

A more detailed evaluation of the constituent intermolecular interactions within the αLMH structure is highlighted in Fig. 6 and detailed in Table 2 (columns 2–7) which lists the top five strongest intermolecular synthons. The calculated synthonic interaction energies are generally in broad agreement with those in the literature[82] with discrepancies most likely being due to the use of different forcefields and atomic charge calculation methods. The top two synthons (A & B) have two HBs, synthons D & E present only one HB and the $\pi - \pi$ stacking synthon C has no HB, with all HBs being the OH ... O interaction. These interactions collectively were found to contribute ~68 % to the total lattice energy.

As expected, the strengths of the lactose–water interactions (synthon E) were much less when compared to those from the lactose –lactose interactions (synthon A, B, C and D) whilst the energies associated with water–water interactions were similarly very low (-0.03 kcal mol^{-1}). Nonetheless, despite their lower interaction energies, it is clear that the water molecules play a vital role within the αLMH bulk crystal chemistry in that they act to bind together with the sheets of lactose molecules which are related by the 2_1 screw axis. This supports the observation that anhydrous lactose when formed by heating tends to rapidly re-absorb water to form the αLMH structure again.[77,78]

Table 2
Top five strongest intermolecular synthons highlighting the individual molecules contributing to these interactions, additionally the synthon energetic contributions to the attachment energy E_{att} for the morphologically important crystal surfaces are provided together with the multiplicity of the contribution to that specific surface.

Synthon	Multiplicity	Molecules Involved	Number of HB	vdW (kcal mol^{-1})	Coulombic (kcal mol^{-1})	Total interaction (kcal mol^{-1})	Top five synthons contributing to E_{att}			
							{020}/{0−20}	{001}	{011}	{0−31}
A	4	LT/LT	2	−3.82	−0.73	−4.55	-	E_{att}	E_{att}	E_{att}
B	4	LT/LT	2	−3.93	−0.55	−4.49	-	E_{att}	E_{att}	E_{att}
C	4	LT/LT	0	−3.69	−0.48	−4.17	-	-	-	-
D	4	LT/LT	1	−1.87	−0.22	−2.09	E_{att}	-	E_{att}	E_{att}
E	4	LT/water	1	−1.57	−0.24	−1.80	E_{att}	-	E_{att}	E_{att}

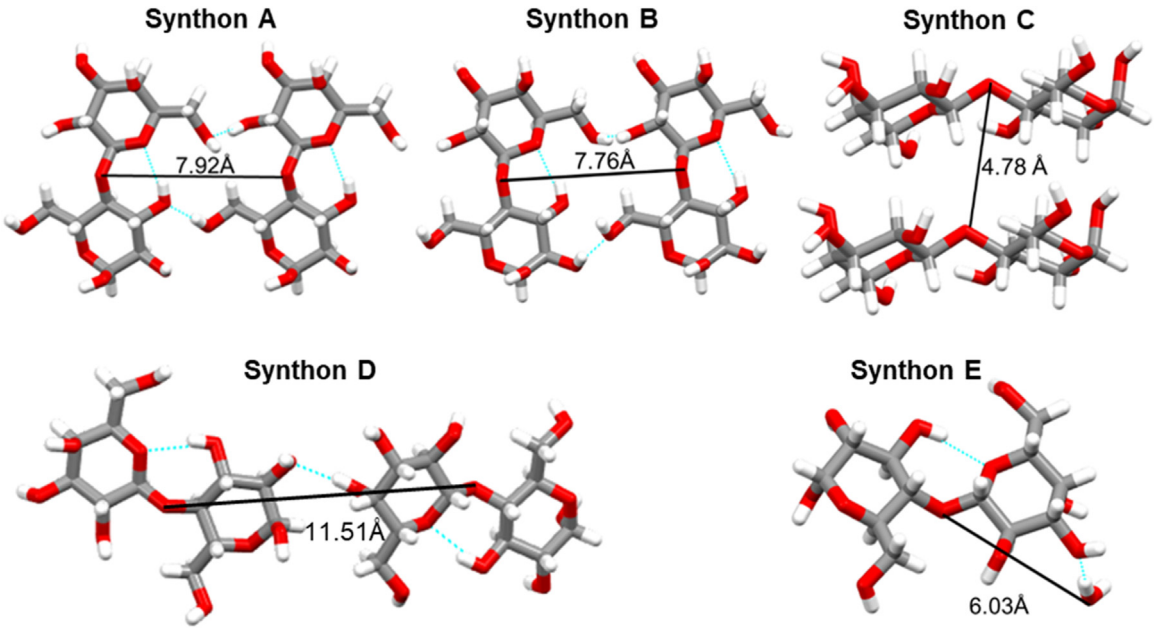

Fig. 6. Molecular diagrams of top five strongest intermolecular synthons with the distances quoted being the distances between the two centers of gravity of the molecules.

Table 3
Analysis of crystal surfaces of αLMH, their attachment energies and surface energy for individual crystal forms.

Face (*hkl*)	d_{hkl} (Å)	Surface Area (%)	E_{sl} (kcal mol^{-1})	E_{att} (kcal mol^{-1})	ξ_{hkl} (%)	Rugosity (-)	Predicted Dispersive SE[a] (mJ m^{-2})	Predicted total SE[b] (mJ m^{-2})
{020}[c]	10.77	17.01	−17.02	−8.01	68.00	1.21	67.38	77.96
{001}	7.46	9.39	−12.73	−12.30	50.86	1.53	71.25	82.92
{0-31}	5.17	5.67	−7.02	−18.01	28.05	1.60	73.32	84.21
{1-1-1}	4.41	5.65	−10.54	−14.49	42.11	1.27	51.06	57.76
{100}[c]	4.60	4.68	−10.81	−14.21	43.19	1.43	51.25	59.10
{1-10}[c]	4.50	3.92	−9.75	−15.28	38.95	1.32	53.99	62.12
{0-11}[c]	7.05	3.60	−10.89	−14.14	43.51	1.46	78.00	90.10
{10-1}	4.51	3.59	−11.22	−13.81	44.83	1.32	49.85	56.24
{0-21}	6.13	2.99	−8.84	−16.19	35.32	1.61	78.05	89.75
{11-1}	4.41	1.31	−10.54	−14.49	42.11	1.28	51.06	57.76
{110}[c]	4.50	0.50	−9.75	−15.28	38.95	1.29	53.99	62.12
{011}	7.05	0.20	−10.89	−14.14	43.51	1.34	77.98	90.09

[a] Predicted dispersive surface is calculated from vdW contributed to E_{att}.
[b] Predicted total surface energy is calculated from E_{att}.
[c] Surfaces are presented in the experimental crystal morphology grown from aqueous solution.

Surface properties

Attachment and surface energies

The calculated surface and attachment energies for the morphologically important forms are presented in Table 3.

Extrinsic synthon analysis

The individual intermolecular extrinsic synthons that contribute to the surface attachment energies, and hence their growth, for a given crystal habit plane surface are listed in Table 2 (column 8–11) with some selected surfaces being summarised in surface chemistry packing diagrams as shown in Fig. 7.

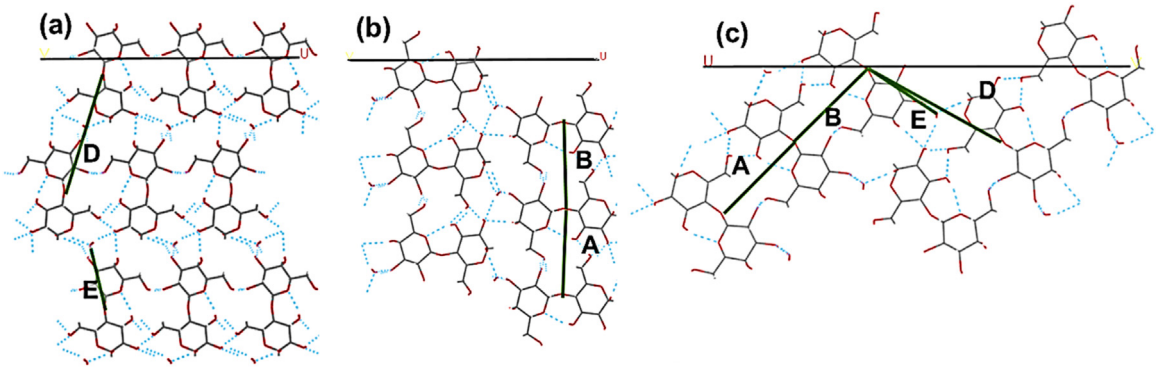

Fig. 7. Molecular orientation for selected crystal habit surfaces: (a) {020} face with synthon D and E contributing to its attachment energy; (b) {001} surface with synthons A and B contributing to its attachment energy; and (c) {0-31} face with synthons A, B, D and E marked as contributing to its attachment energy.

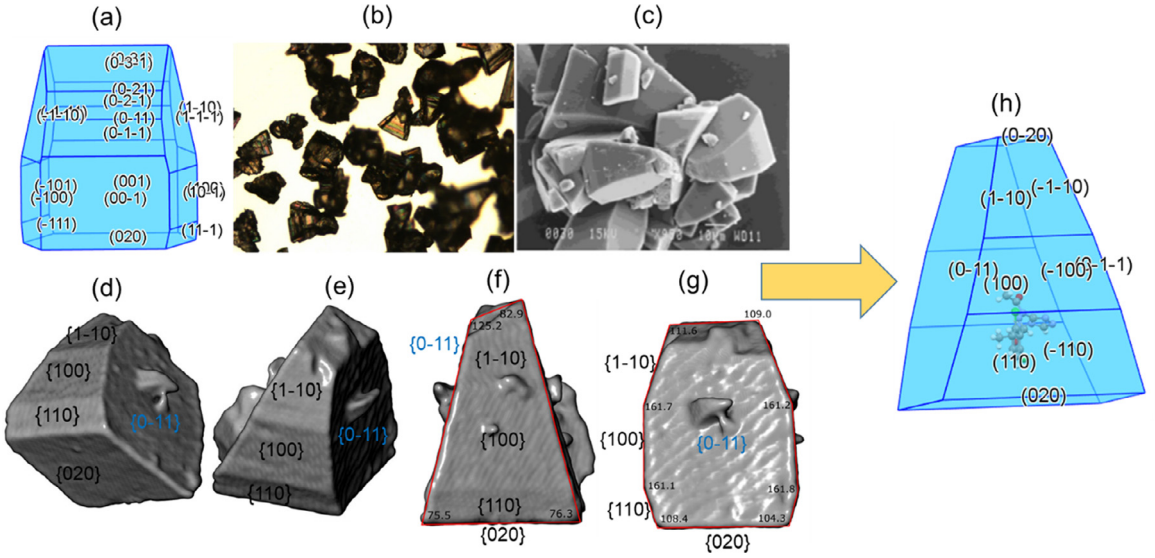

Fig. 8. Predicted and experimental morphology of αLMH: (a) Predicted morphology (excluding the (0−20) surface due to the polar effect of the monoclinic space group $P2_1$ correctly reproduced by the presence of only one of the {020} form); (b) αLMH grown in water from this study; (c) The morphology of αLMH crystals precipitated from aqueous solutions at the supersaturation 130 %,[10] (d−g) 3D experimental crystal growth morphology characterised by LabDCT, together with crystal faces indexed based on the calculated and the measured interfacial angles of the real crystal morphology; (h) Modified prediction of the crystal morphology (a) to match that recorded in 3D by LabDCT (d−g).

Fig. 7 highlights that, for the {020} form, the strongest intermolecular interactions, i.e. highest contribution to the attachment energy, were synthons D and E, representing the interactions between two lactose molecules and lactose-water molecules, respectively. Whilst synthon A (strongest synthon) and synthon B both contribute to the slice energy for the capping {020} surface but they also contribute to the attachment energy for the prismatic {001}, and {0-31} surfaces. These are consistent with the observed morphological importance of {020} > {001} > {0-31}.

Surface chemistry

Morphological analysis using the BFDH method reveals the dominant forms for αLMH would be expected to be (020), (0-20), (001), (011) and (031). The surface chemistry associated with these surfaces is shown in **Fig. S1** (SI). The intermolecular packing for all these crystal habit surfaces (**Fig. S1** (SI)) demonstrates that the lactose molecules are oriented with their ring planes vertically and aligned with respect to the b-axis within the dominant {010}, {001}, {011}, {0-11}, {0-21}, and {0-31} surfaces. For the less morphologically dominant {100}, {110} and {1-10} surfaces, they are oriented horizontally. Analysis of the bulk solid-state interactions showed that the dominant intermolecular interactions mostly result from dispersive vdW intermolecular interactions. Hence, the surfaces displaying molecules arranged in the horizontal orientation perpendicular to the growth surface would be expected to maximise the strength of the dispersive interactions as this more favourable molecular orientation for intermolecular interactions and one that would result in a higher surface attachment energy, hence higher expected growth rate and concomitantly smaller surface area.

Particle properties

Predicted morphology

The predicted morphology based on the attachment energy data in Table 3 is shown in Fig. 8(a) alongside the experimental morphology of αLMH (Fig. 8(b−g)).

Predicted crystal morphology in comparison with experimental data

The predicted morphology highlights the dominant {020}, {110}, {0-11}, {100} and {1-10} crystal habit forms in broad agreement with previous studies,[46] as well as with those crystallised from aqueous solution in this study (Fig. 8(b−g)). It is noteworthy that the latter displays an overall polar prismatic morphology associated with a characteristic tomahawk habit (Fig. 8(b−g)), leading to the modification of the predicted morphology (Fig. 8(a)) to match the experimental one (Fig. 8(d−g)) for calculations of surface energies based on

Table 4
Interaction (binding) energies (in kcal/mol^{-1}) of β-lactose on four possible surface terminations (T1 – T4) of the (010) and (0-10) crystal surfaces of αLMH. Note that the four face terminations are shown in **Figs. S2** and **S3** (SI).

Crystal surface of αLMH		(010)				(0-10)			
Type	Termination	vdW	H-bond	Coulombic	Total	vdW	H-bond	Coulombic	Total
Water layer	T1	−5.51	−10.87	−1.15	−17.44	−5.65	−6.39	−0.31	−12.36
No water layer at the surface	T2	−4.13	−8.45	−1.65	−14.22	−4.60	−7.96	−1.02	−13.59
Alternative water layer	T3	−6.40	−9.29	−1.25	−16.94	−5.27	−7.15	−0.53	−12.95
Alternative of no water layer at the surface	T4	−3.81	−9.35	−1.57	−14.73	−5.84	−5.47	−0.96	−12.27
Average of four terminations		−4.96	−9.49	−1.41	−15.83	−5.32	−6.74	−0.71	−12.79

(Fig. 8(h)). The {020} form had the lowest attachment energy and highest percentage of satisfied synthons at the surface (ξ = 0.66) (see column 6 in Table 3) and therefore was predicted to be the slowest growing face of αLMH, which was in good agreement with the tomahawk-like, triangle morphology with dominant {020} and {001} forms.

It is important to note that the attachment energy simulations do not (cannot) directly simulate the polar nature of the (010)/(0-10) forms, hence further analysis is needed. Specifically the {010} form represents polar faces where the molecular packing arrangements are different for the two surfaces (010) and (0-10) confirming that αLMH is a polar crystal. In the predicted morphology the (010) face has the highest surface area (the dominant face), followed by the (001) face. The (010) and (0-10) surfaces are not symmetry related due to lack of any centre of inversion in the $P2_1$ structure, hence the (010) and (0-10) faces produced different surface compositions. The molecular arrangement of these two faces has considerable influence on the surface energetics of the whole facetted crystal. The molecular arrangement of all these faces also clarifies the basicity of the surface due to the presence of different negatively charged oxygen atoms or the delocalised electrons on the ring structure, present on the surface.[83]

A simple morphological analysis of αLMH using the BFDH[61–63] crystal lattice geometric rules reveals a base-line crystal habit (Fig. S4 (SI)) that is rather tabular plate-like in nature and one that is dominated by the slow growing {010} and {0-10} planes. This morphology closely resembles crystals prepared by crystallisation from aprotic solvents such as dimethyl sulfoxide (DMSO).[9] There are two questions that then follow from this.

- Why is the observed crystal morphology of αLMH when it is crystallised from aqueous solutions elongated along the slow growing capping face (b-axis) of the crystal.
- Why do the crystals display a tomahawk-shaped prismatic polar morphology with distinctly different growth rates observed for the polar {010} and {0-10} growth surfaces.

Effect of aqueous solvent binding on the different crystal habit surfaces

A comprehensive examination of the surface chemistry for the polar {010} and equatorial {110}, {0-11}, {100} and {1–10} facets reveals that the polar facets have a much lower density of hydrogen bond binding sites (see Figs. S5–S9 (SI)) when compared to the equatorial facets in aqueous solutions. The latter can be expected to be highly effective in terms of binding protic solvent molecules when compared to the polar facets where density is much lower. The polar facets also form the binding sites for the monohydrate's solid-state hydration water molecules where they assemble an inter-laminae layer sandwiched between the lactose molecules. A further factor lies in the fact that the molecular-scale roughness of the polar faces is much less than for the prismatic faces which would supports strong surface binding of solvent molecules to the prismatic faces where their rougher surface topology allied to lack of hydration water molecules and predominance of hydration binding sties could be expected to optimal for adsorption when compared to the molecularly flatter capping faces. Such a differential binding behavior would be consistent with the observed elongated morphology along the b-axis when αLMH is crystallised from aqueous solutions whereby crystal growth would be expected to be more inhibited by desolvation on the prismatic with respect to the capping facets. Such a model would also be fully consistent with the observed plate-like morphology that has been observed in αLMH when it has been crystallised from aprotic solvents such as DMSO.[9]

Absolute polarity of αLMH polar {010} and {0-10} surfaces through examining β-lactose binding

Close examination of the surface chemistry of the {010} and {0-10} polar forms reveals that there are four different potential surface terminations (either lactose molecules or water molecules exposed on the crystal surface) for these {010} and {0-10} crystal habit surfaces. Such differences in surface termination and water molecules' position can directly affect the interaction of hetero-species within the crystallisation environment with other functional groups present on the surface. It is well-known that the presence of β-lactose can be a key factor in mediating crystal morphology for αLMH as it can selectively block the growth of either the {010} or {0-10} faces, resulting in the growth of the asymmetric "tomahawk" crystal habit. This results overall in the (0-10) face becoming less dominant than that of the (010) or vice versa. The calculated intermolecular interaction (binding) energies of β-lactose for the different surface terminations (T1 – T4) of the (010) and (0-10) crystal surfaces of αLMH is

Table 5
Measured and published surface energies for various grade of αLMH.

αLMH grade	Dispersive SE (mJ m^{-2})	Total SE (mJ m^{-2})	Polar SE (mJ m^{-2})	References
Calculated particle surface energy (average weighted with % surface area)	64.0	73.7	9.7	Calculated in this study (Eq. (4))
Sieved lactose (Lactohale 100) (with surface coverage from 1% to 20%)	39.8–43.9	67.2–81.7	27.4–37.8	Measured in this study
Coarse-grade αLMH (batch no. 120904-25, Pfizer Global Research & Development)	65.3	77.6	12.3	Ramachandran, V. et al.[25]
Milled lactose*	53.0	62.2	9.2	Thielmann, F. et al.[84]
Recrystallised lactose*	~42.0	49.2	~7.2	Thielmann, F. et al.[84]
Untreated lactose*	~43.0	53.7	~10.7	Thielmann, F. et al.[84]

* 0% coverage corresponding to infinite dilution conditions.

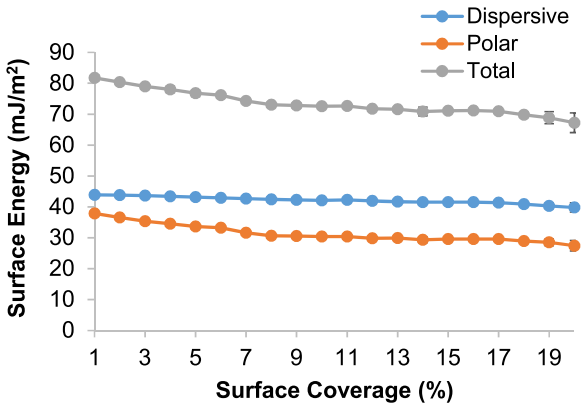

Fig. 9. Measured dispersive and total surface energy of αLMH determined by IGC showing the surface energy decrease with increasing surface coverage.

given in Table 4 with their preferential binding positions of β-lactose molecule on the two αLMH habit surface being shown in **Figs. S2** and **S3** (SI).

Overall, the surface binding data shows that β-lactose molecules have stronger binding with the (010) crystal surface of αLMH than for the (0-10) face for all four different types of surface terminations. The vdW interactions for the (010) were though found to be slightly weaker than those for the (0-10), whilst the hydrogen bond interactions for the (010) surface were much higher than for the (0-10). For example, for the (010) crystal surface with the surface termination 1 (the presence of water on the crystal surface), the hydrogen bonds contribute −10.87 kcal mol^{-1} (62.3 % of total binding energy), whilst for the (0-10) surface, the hydrogen bonds contribute −6.39 kcal mol^{-1} (51.7 % of total binding energy). In the αLMH structure, the lactose molecules are oriented with their long axis parallel to the b axis with the glucose moieties pointing towards the [0-10] direction, hence the β-lactose molecules can be incorporated in the crystal lattice on the (010) faces to inhibit their growth.

Visualisation of the strongest interaction of β-lactose on the surfaces (**Figs. S2** and **S3** (SI)) shows that the most favoured orientation at the {010} and {0-10} co-ordinates with four different surfaces terminations were in different orientations. In terms of molecular orientation, the β-lactose was found to lie flat on the (0-10) crystal surface whereas on the (010) surface of the β lactose, this was not the case. Overall, the binding analysis shows that β-lactose has a significantly stronger interaction energy on the (010) when compared to the (0-10) surfaces for all four of the surface terminations. Importantly, there were a higher number of possible hydrogen bonding interactions for β-lactose on the (010) surface than for the (0-10) surface, consistent with the higher hydrogen bond interaction energy calculated for the (010) surface. In summary, β-lactose molecules had much stronger binding interactions with the (010) surface than for the (0-10) surface, consistent with the growth of the (010) surface being impeded through impurity incorporation, hence having a lower growth rate than the (0-10) surface. This results in the (010) surface being more morphologically dominant than the (0−10) face, leading, in turn, to the observed tomahawk polar crystal morphology.

Surface area weighted surface energy of the facetted particle

The predicted cumulative surface energies calculated using Eq. (4) and the measured surface energies of αLMH, as measured by IGC, are reported in Table 5 and Fig. 9, respectively. The calculated surface area weighted particle surface energy was 73.7 mJ m^{-2}, which is comparable to that measured by IGC (with surface coverage from 1 % to 20 %) with ranges between 67.2 and 81.7 mJ m^{-2} for sieved lactose (Lactohale 100) and the previously published surface energies[25,84] for various grade of αLMH. Note that the fundamental differences between the environments underpinning the experimental measurements (positive pressure) and predictions (vacuum) may result in the deviation of the measurements from calculations.[85] In future work, to more closely represent the real conditions under IGC measurement conditions, heteromolecular contaminations (e.g. water) and/or imperfections (such as amorphous) may be introduced to the habit faces, hence reducing the deviation between the predicted and measured surface energies.

Table 3 (column 9) shows the calculated surface energy of individual crystal faces being broken down into dispersive SE (column 8). The dispersive particle SE, calculated using Eq. (4) based upon the surface-area weighted summation of the individual predicted crystal surface energies, has value of 64.0 mJ m^{-2} (Table 5, column 2). This value is in good agreement with the measured dispersive SE of 65.3 mJ m^{-2} for the coarse-grade lactose monohydrate[25]; however it is higher than that measured for the sieved lactose (Lactohale 100; DFE Pharma (GmbH)) used in this study. However, the measured surface energy values reported in previous studies have been known to vary depending on the sample preparation methods, as well as on the measurement conditions.[84,86–88] The calculated surface energies of individual surfaces (Table 3) reveal that the surface energies of the facetted αLMH crystal habit surfaces were quite uniform (average deviation being around 19 %), which might be expected to be the case mindful that αLMH provides an important candidate for use as an excipient in practical drug formulation. The low variations between d_{hkl} and E_{att} for the individual surfaces, hence their growth rates and surface energies, could be expected to lead to the high

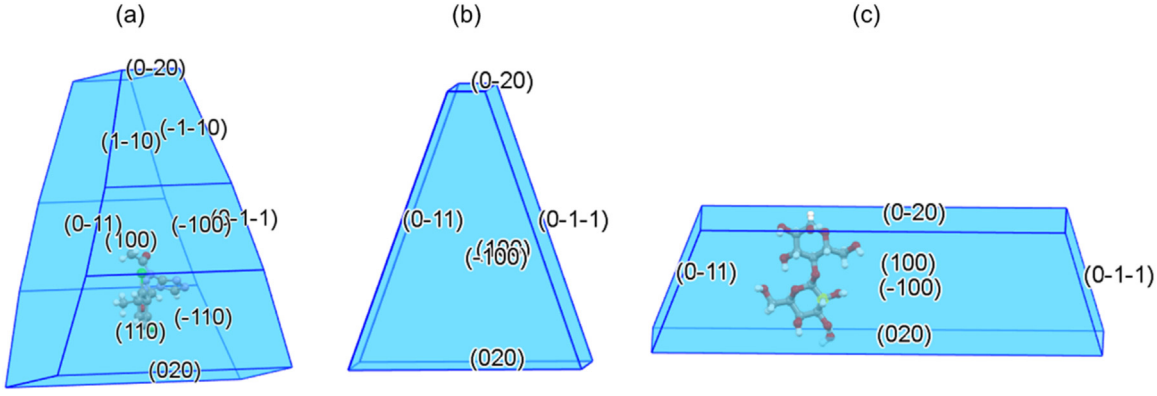

Fig. 10. Predicted crystal morphology of αLMH adapted according to the observed crystal morphology grown in various conditions (a) tomahawk crystal morphology of αLMH grown from water at low supersaturation (33–43 % w/w), (b) triangle-shape crystal grown in medium supersaturation (50 % w/w) solution and (c) elongated-shape of crystal grown from water at high supersaturations (60 % w/w) and from DMSO solution.[9,89]

Table 6
Calculated crystal surfaces of αLMH, their surface area and surface energy for individual crystal forms for tomahawk, triangle and needle-like crystals.

Crystal surfaces	Tomahawk shaped crystal habit		Triangular shaped crystal habit		Elongated tabular shaped crystal habit	
	Surface Area (%)	SE (mJ m^{-2})	Surface Area (%)	SE (mJ m^{-2})	Surface Area (%)	SE (mJ m^{-2})
{020}	15.4	78.0	18.2	77.9	26.6	77.9
{0-20}	3.5	340.7	2.9	340.7	21.5	107.1
{0-11}	41.6	101.9	16.0	59.0	18.3	59.0
{100}	11.8	56.1	16.0	59.0	18.3	59.0
{110}	18.0	48.8	23.4	90.2	7.7	90.2
{1-10}	9.8	69.1	23.4	90.2	7.7	90.2
Total SE weighted with % of surface area (mJ m^{-2})		88.5		85.3		79.2

degree of homogeneity (< 20 % variation) of αLMH surface energies (Table 3, column 9). For the {020} surface, the high variations of d_{hkl} (83 %) and E_{att} (−44 %) compensate to produce a calculated surface energy which is similar to the other surfaces.

Particle surface energies for different crystal habits and their impact on formulation

It is well known that the morphology of αLMH crystals can vary when prepared from different growth environments associated with a variation in the relative growth rates between its constituent crystal-habit faces. Ultimately, such a variation can be linked to the respective interaction energies associated with the strongest extrinsic synthons important in the growth environment in the development of these surfaces. In aqueous solutions, at low (33–43 % w/w), medium (50 % w/w) and high supersaturations (60 % w/w), αLMH recrystallises with a tomahawk or pyramid-shape, a prismatic shape and more elongated particles, respectively[12] whilst crystallisation from dimethyl sulfoxide (DMSO), an aprotic polar solvent, has been observed to suppress the polar morphology. The latter has also been used to study the effect of β-lactose on the morphology of αLMH crystals, this solvent has been known to greatly reduces the mutarotation rate between α-lactose and β-lactose. At low concentrations of β-lactose within the growth solution, the fastest growing face of the α-lactose crystals is {0-11}, resulting in long thin prismatic crystals. At higher β-lactose concentrations, the main growth occurs in the positive [0-10] direction of the crystal with the {0-10} face becoming the fastest growing face as the (010) face is inhibited by β-lactose, producing pyramid and tomahawk shaped crystals.[9] Fig. 10 shows morphological representation of αLMH representing the experimental crystal morphology in various conditions whilst the associated calculated crystal surface areas of αLMH, attachment energies and surface energies for tomahawk, triangle and needle-like crystals are given in Table 6.

Analysis of these predicted particle surface energies after surface area-weighting suggests that the particle surface energy changes in the rank order of tomahawk > triangle > elongated, albeit with differences of just 4–9 mJ m^{-2}.

For both drug tested budesonide and fluorescein, the milled lactose carriers (more crystalline in shape, lower surface energy) provide significantly improved performance over the spray dried lactose (spherical, higher surface energy) of the blended powder.[26] When the surface energy of αLMH is increased, the dry powder inhaler was less efficient in terms of aerosol performance regarding the drug detachment from the αLMH particle carrier.[26, 27] This is assumed to be partly due to a rise in the surface energy, which results in the force of adhesion becoming higher making it harder for the drug particles to de-agglomerate.[90] This would be consistent with the findings in this study in that the elongated αLMH crystals have lower surface energies when compared to the tomahawk ones. Hence, as a result, it should be expected to exhibit a better aerosol dispersion performance. The prediction of the strength of cohesive and adhesive interparticle interactions for dry powder inhalation blends of TSB and αLMH crystal revealed that the surface-surface interaction energies of αLMH faces, e.g. {010}-{010}, {010}-{0-11}, {0-11}-{0-11} and {0-11}-{010}, were quite homogeneous.[44] This is consistent with the findings in this study, with αLMH being known to be a good excipient candidate for routine use within drug formulations.

Conclusions

A detailed analysis of the molecular, intermolecular, solid-state and surface chemistry of αLMH has been presented highlighting their inter-connectivity with the material's physical chemical properties, notably its cohesive and adhesive behaviour within formulations. Synthonic modelling revealed the extent and importance of vdW intermolecular interactions which account for ca. 85 % of the lattice energy of αLMH with the strongest synthons being associated with intermolecular interactions between the lactose-lactose pairs, stronger binding of solvation water molecules to the prismatic compared to the polar surfaces result in enhanced growth along the long b-axis of the αLMH structure. Predicted crystal morphologies were found to be in good agreement with XCT characterisation of 3D experimental morphological data. Asymmetric surface binding between β-lactose on the (010) and (0-10) polar faces confirms its enhanced binding to the (010) faces rationalising the characteristic tomahawk morphology observed for αLMH.

Overall, the calculated surface energies agreed well with those measured by IGC. The predicted whole particle surface energy as a function of crystal morphology has shown the elongated crystal morphology to have a lower surface energy compared to the tomahawk morphology, consistent with experimental observations that the particle surface energies of the lactose carriers are inversely proportional to its aerosol dispersion performance. The ability to predict particle surface energy can form a key part of a digital design workflow to inform the design of formulated drug products for inhaled medicines in order to maintain effective drug aerosolization in delivery devices, hence providing direct benefit for inhaled[25,44] medicine design and delivery.

More generally, analysis is potentially helpful for assessing and interpreting measured IGC data, through the prediction's ability to distinguish surface energies between different morphological forms, and hence the surface chemistry of different crystal habit planes. Such surface energy data can be correlated to inter-particulate adhesive and cohesive interactions within agglomerated powdered products.

Overall, this study would suggest that the *in-silco* calculated surface energy presented here might also have more general applications in the formulation design of other APIs and formulation routes in order to understand the effect of physical properties on the manufacturability and performance of drug products.

List of symbols and abbreviations

A_i^{hkl}: Fractional surface area of the habit face
d_{hkl} : Inter-planar spacing
E_{cr}: Lattice Energy
E_{slice} : Slice Energy
E_{att}^{hkl}: Attachment Energy
M_i^{hkl}: Multiplicity of the crystallographically equivalent habit faces
n: Number of forms (family of faces)
R: Molar gas constant
T: Temperature
Z: Number of molecules per unit cell
ΔH_{sub}: Experimental sublimation enthalpy
γ_{disp}: Dispersive component of surface energy
γ_{es}: Electrostatic component of surface energy
$\gamma_{particle}$: Overall particle surface energy
γ_i^{hkl}: Surface energy of individual crystal surface
ξ_{hkl} : Anisotropy factor
API: Active pharmaceutical ingredient
CSD: Cambridge Structural Database
IGC: Inverse gas chromatography
LabDCT: Laboratory diffraction contrast tomography
SE: Surface Energy
TBS: Terbutaline sulfate vdW: van der Waals
XCT: X-ray computed tomography
αLMH: α-lactose monohydrate

Data availability

The data that support the findings of this study are available from the corresponding author (KJR) upon reasonable request.

Declaration of competing interest

The authors declare that they have no known competing financial interests or personal relationships that could have appeared to influence the work reported in this paper.

Acknowledgements

This work was supported by the UK's EPSRC research grant (EP/N025075/1): INFORM2020 "Molecules to Manufacture: Processing and Formulation Engineering of Inhalable Nanoaggregates and Micro-Particles". This work also builds upon research on morphological modelling supported by EPSRC grant (EP/I028293/1): 'HABIT – Crystal morphology from crystallographic and growth environment factors', the Synthonic Engineering programme supported by Pfizer, Boeringer-Ingellheim, Novartis and Syngenta, and ADDOPT project (Grant No. 14060) in collaboration with Dr Jonathan Pickering at Leeds for software developments. X-ray tomographic beam time was kindly provided by the Henry Moseley X-ray Imaging Facility (HMXIF), which was established through EPSRC grants EP/F007906/1, EP/I02249X/1, and EP/F028431/1 and which now forms part of the National Facility for Laboratory X-ray CT funded through EPSRC Grant EP/T02593X/1. HMXIF is also a part of the Henry Royce Institute for Advanced Materials, established through EPSRC grant nos. EP/R00661X/1, EP/P025498/1, and EP/P025021/1.

Supplementary materials

Supplementary material associated with this article can be found, in the online version at doi:10.1016/j.xphs.2024.10.031.

References

1. Spahn JE, Zhang F, Smyth HDC. Mixing of dry powders for inhalation: a review. *Int J Pharm*. 2022;619: 121736.
2. Fox P. *Lactose: Chemistry and properties*. Advanced Dairy Chemistry. Springer; 2009:1–15.
3. Holsinger VH. *Lactose. Fundamentals of Dairy Chemistry*. Springer; 1988:279–342.
4. Visser RA. *Crystal Growth Kinetics of Alpha-Lactose Hydrate*. Nijmegen: Radboud University; 1983.
5. Garnier S, Petit S, Coquerel G. Dehydration mechanism and crystallisation behaviour of lactose. *J Therm Anal Calorim*. 2002;68:489–502.
6. Smith JH, Dann SE, Elsegood MR, Dale SH, Blatchford CG. α-lactose monohydrate: a redetermination at 150 K. *Acta Crystallogr Sect E: Struct Rep*. 2005;61(8). o2499-o2501.
7. Hebbink G.A., Dickhoff B.H.J. Chapter 5 - Application of Lactose in the Pharmaceutical Industry. In: Paques M, Lindner C, (eds.) *Lactose: Evolutionary Role, Health Effects, and Applications*. Academic Press; 2019:175–229, ISBN 978-170-112-811720-811720.
8. Michaels AVK. A. Influences of additives on growth rates in lactose crystals. *Netherlands Milk Dairy J*. 1966;20(3):163–181.
9. Dincer TD, Parkinson GM, Rohl AL, Ogden MI. Crystallisation of α-lactose monohydrate from dimethyl sulfoxide (DMSO) solutions: influence of β-lactose. *J Cryst Growth*. 1999;205(3):368–374. https://doi.org/10.1016/S0022-0248(99)00238-9.
10. Raghavan SL, Ristic RI, Sheen DB, Sherwood JN. The bulk crystallization of α-lactose monohydrate from aqueous solution. *J Pharm Sci*. 2001;90(7):823–832. https://doi.org/10.1002/jps.1036.
11. Parimaladevi P, Srinivasan K. Influence of supersaturation level on the morphology of α-lactose monohydrate crystals. *Int Dairy J*. 2014;39(2):301–311.
12. Zeng XM, Martin GP, Marriott C, Pritchard J. The influence of crystallization conditions on the morphology of lactose intended for use as a carrier for dry powder aerosols. *J Pharmacy Pharmacol*. 2000;52(6):633–643.
13. Zeng XM, Pandhal KH, Martin GP. The influence of lactose carrier on the content homogeneity and dispersibility of beclomethasone dipropionate from dry powder aerosols. *Int J Pharm*. 2000;197(1–2):41–52.
14. Zeng XM, Martin GP, Marriott C, Pritchard J. Lactose as a carrier in dry powder formulations: the influence of surface characteristics on drug delivery. *J Pharm Sci*. 2001;90(9):1424–1434. https://doi.org/10.1002/jps.1094.
15. Dickhoff B, De Boer A, Lambregts D, Frijlink H. The effect of carrier surface and bulk properties on drug particle detachment from crystalline lactose carrier particles during inhalation, as function of carrier payload and mixing time. *Eur J Pharm Biopharm*. 2003;56(2):291–302.
16. Le VNP, Bierend H, Robins E, Steckel H, Flament MP. Influence of the lactose grade within dry powder formulations of fluticasone propionate and terbutaline sulphate. *Int J Pharm*. 2012;422(1):75–82. https://doi.org/10.1016/j.ijpharm.2011.10.030.
17. Marriott C, Frijlink HW. Lactose as a carrier for inhalation products: breathing new life into an old carrier. Preface. *Adv Drug Deliv Rev*. 2012;64(3):217–219.
18. Zhou QT, Morton DA. Drug–lactose binding aspects in adhesive mixtures: controlling performance in dry powder inhaler formulations by altering lactose carrier surfaces. *Adv Drug Deliv Rev*. 2012;64(3):275–284.
19. van Kreveld A, Michaels AS. Measurement of crystal growth of α-lactose. *J Dairy Sci*. 1965;48(3):259–265.
20. Panakanti R, Narang AS. *Impact of Excipient Interactions on Drug Bioavailability from Solid Dosage forms*. Excipient Applications in Formulation Design and Drug Delivery. Springer; 2015:273–310.
21. Jaffari S, Forbes B, Collins E, Khoo J, Martin GP, Murnane D. Evidence for the existence of powder sub-populations in micronized materials: aerodynamic size-fractions of aerosolized powders possess distinct physicochemical properties. *Pharm Res*. 2014;31(12):3251–3264.
22. Malcolmson RJ, Embleton JK. Dry powder formulations for pulmonary delivery. *Pharm Sci Technol Today*. 1998;1(9):394–398.
23. Telko MJ, Hickey AJ. Dry powder inhaler formulation. *Respir Care*. 2005;50(9):1209–1227.
24. Nguyen TTH, Hammond RB, Styliari ID, Murnane D, Roberts KJ. A digital workflow from crystallographic structure to single crystal particle attributes for predicting the formulation properties of terbutaline sulfate. *CrystEngComm*. 2020;22:3347–3360.
25. Ramachandran V, Murnane D, Hammond RB, et al. Formulation pre-screening of inhalation powders using computational atom–atom systematic search method. *Mol Pharm*. 2015;12(1):18–33.
26. Saleem I, Smyth H, Telko M. Prediction of dry powder inhaler formulation performance from surface energetics and blending dynamics. *Drug Dev Ind Pharm*. 2008;34(9):1002–1010.
27. Traini D, Young PM, Thielmann F, Acharya M. The influence of lactose pseudopolymorphic form on salbutamol sulfate–lactose interactions in DPI formulations. *Drug Dev Ind Pharm*. 2008;34(9):992–1001.
28. Zeng XM, Martin GP, Marriott C, Pritchard J. The influence of carrier morphology on drug delivery by dry powder inhalers. *Int J Pharm*. 2000;200(1):93–106.
29. Kaialy W, Ticehurst MD, Murphy J, Nokhodchi A. Improved aerosolization performance of salbutamol sulfate formulated with lactose crystallized from binary mixtures of ethanol—acetone. *J Pharm Sci*. 2011;100(7):2665–2684. https://doi.org/10.1002/jps.22483.
30. Begat P, Morton DA, Staniforth JN, Price R. The cohesive-adhesive balances in dry powder inhaler formulations I: direct quantification by atomic force microscopy. *Pharm Res*. 2004;21(9):1591–1597.

31. Kho K, Hadinoto K. Dry powder inhaler delivery of amorphous drug nanoparticles: effects of the lactose carrier particle shape and size. *Powder Technol*. 2013;233:303–311. https://doi.org/10.1016/j.powtec.2012.09.023.
32. Docherty R, Clydesdale G, Roberts KJ, Bennema P. Application of the Bravais-Friedel-Donnay-Harker, attachment energy and Ising models to predicting and understanding the morphology of molecular crystals. *J Phys D: Appl Phys*. 1991;24:89–99.
33. Anuar N, Wan Daud WR, Roberts KJ, Kamarudin SK, Tasirin SM. Morphology and associated surface chemistry of Lisoleucine crystals modeled under the influence of L-leucine additive molecules. *Cryst Growth Des*. 2012;12:2195–2203.
34. Clydesdale G, Roberts KJ, Docherty R. Modelling the morphology of molecular crystals in the presence of disruptive tailormade additives. *J Cryst Growth*. 1994;135:331–340.
35. Smith LA, Duncan A, Thomson GB, Roberts KJ, Machin D, McLeod G. Crystallisation of sodium dodecyl sulphate from aqueous solution: phase identification, crystal morphology, surface chemistry and kinetic interface roughening. *J Cryst Growth*. 2004;263:480–490.
36. Hammond RB, Pencheva K, Roberts KJ. Molecular modeling of crystal−crystal interactions between the α- and β-polymorphic forms of L-glutamic acid using grid-based methods. *Cryst Growth Des*. 2007;7(5):875–884. https://doi.org/10.1021/cg0605234.
37. Hammond RB, Jeck S, Ma CY, Pencheva K, Roberts KJ, Auffret T. An examination of binding motifs associated with inter-particle interactions between facetted nanocrystals of acetylsalicylic acid and ascorbic acid through the application of molecular grid-based search methods. *J Pharm Sci*. 2009;98(12):4589–4602. https://doi.org/10.1002/jps.21758.
38. Moldovan AA, Rosbottom I, Ramachandran V, et al. Crystallographic structure, intermolecular packing energetics, crystal morphology and surface chemistry of salmeterol xinafoate (form I). *J Pharm Sci*. 2017;106:882–891.
39. Turner TD, Hatcher LE, Wilson CC, Roberts KJ. Habit modification of the active pharmaceutical ingredient lovastatin through a predictive solvent selection approach. *J Pharm Sci*. 2019;108:1779–1787.
40. Wang C, Rosbottom I, Turner TD, et al. Molecular, solid-state and surface structures of the conformational polymorphic forms of ritonavir in relation to their physicochemical properties. *Pharm Res*. 2021;38:971–990.
41. Hammond RB, Ma CY, Roberts KJ, Ghi PY, Harris RK. Application of systematic search methods to studies of the structures of urea−dihydroxy benzene cocrystals. *J Phys Chem B*. 2003;107(42):11820–11826. https://doi.org/10.1021/jp035010b.
42. Hammond RB, Hashim RS, Ma CY, Roberts KJ. Grid-based molecular modeling for pharmaceutical salt screening: case example of 3,4,6,7,8,9-hexahydro-2H-pyrimido (1,2-a) pyrimidinium acetate. *J Pharm Sci*. 2006;95(11):2361–2372. https://doi.org/10.1002/jps.20657.
43. Rosbottom I, Pickering J, Etbon B, Hammond R, Roberts K. Examination of inequivalent wetting on the crystal habit surfaces of RS-ibuprofen using grid-based molecular modelling. *Phys Chem Chem Phys*. 2018;20(17):11622–11633.
44. Ma CY, Nguyen TTH, Gajjar P, et al. Predicting the strength of cohesive and adhesive interparticle interactions for dry powder inhalation blends of terbutaline sulfate with α-lactose monohydrate. *Mol Pharm*. 2023;20:5019–5031.
45. Rohl A, Gay D. Calculating the effects of surface relaxation on morphology. *J Cryst Growth*. 1996;166(1−4):84–90.
46. Clydesdale G, Roberts KJ, Telfer GB, Grant DJ. Modeling the crystal morphology of α-lactose monohydrate. *J Pharm Sci*. 1997;86(1):135–141.
47. Lukman Z, Anuar N, Bakar NFA, Rahman NA. Alpha lactose monohydrate morphology: molecular modelling and experimental approach. *Int J Eng Technol (UAE)*. 2018;7(4):107–112.
48. Gajjar P, Styliari ID, Legh-Land V, et al. Microstructural insight into inhalation powder blends through correlative multi-scale X-ray computed tomography. *Eur J Pharm Biopharm*. 2023;191:265–275.
49. Gajjar P, Nguyen TTH, Sun J, et al. Crystallographic tomography and molecular modelling of structured organic polycrystalline powders. *CrystEngComm*. 2021;23:2520–2531.
50. Nguyen TTH, Gajjar P, Sun J, et al. Understanding the agglomerate crystallisation of hexamine through X-ray microscopy and crystallographic modelling. *J Cryst Growth*. 2023;603. No. 126986.
51. Pickering J., Hammond R.B., Ramachandran V., Soufian M., Roberts K.J. Synthonic engineering modelling tools for product and process design. Chapter 10. In: K.J. Roberts RDaRT, ed. *Engineering Crystallography: From Molecule to Crystal to Functional Form*. Springer Advanced Study Institute (ASI) Series; 2017:155−176, ISBN 878-194-024-1118-1118/1115-1117/1117-1111, 2017.
52. Dassault Systèmes. BIOVIA Materials Studio 2019 (https://www.3ds.com/products-services/biovia/products/molecular-modeling-simulation/biovia-materials-studio/), 78946 Vélizy-Villacoublay Cedex, France. 2019.
53. Macrae CF, Sovago I, Cottrell SJ, et al. Mercury 4.0: from visualization to analysis, design and prediction. *J Appl Cryst*. 2020;53:226–235.
54. Ma CY, Moldovan AA, Maloney AGP, Roberts KJ. Exploring the CSD drug subset: an analysis of lattice energies and constituent intermolecular interactions for the crystal structures of pharmaceuticals. *J Pharm Sci*. 2023;112:435–445.
55. Beck AD. Density-functional thermochemistry. III. The role of exact exchange. *J Chem Phys*. 1993;98(7). 5648-5646.
56. Lee C, Yang W, Parr R. *Phys. Re V. B*. 1988;37:785–789.
57. Dovesi R, Erba A, Orlando R, et al. Quantum-mechanical condensed matter simulations with CRYSTAL. *WIREs Comput Mol Sci*. 2018;8(4):e1360. https://doi.org/10.1002/wcms.1360.
58. Clydesdale G, Roberts K, Docherty R. HABIT95—A program for predicting the morphology of molecular crystals as a function of the growth environment. *J Cryst Growth*. 1996;166(1−4):78–83.
59. Stewart JJ. MOPAC: a semiempirical molecular orbital program. *J. Comput. Mol. Des.*. 1990;4(1):1–103.
60. Momany FA, Carruthers LM, McGuire RF, Scheraga HA. Intermolecular potentials from crystal data. III. Determination of empirical potentials and application to the packing configurations and lattice energies in crystals of hydrocarbons, carboxylic acids, amines, and amides. *J Phys Chem*. 1974;78(16):1595–1620. https://doi.org/10.1021/j100609a005.
61. Bravais A. Études Cristallographiques. Paris: Gauthier-Villard; 1913.
62. Friedel G. Leçon de Cristallographie. Paris: Hermann; 1911.
63. Donnay JD, Harker D. A new law of crystal morphology extending the law of Bravais. *Am Mineral*. 1937;22:446–447.
64. Hammond RB, Pencheva K, Roberts KJ. A structural-kinetic approach to model face-specific solution/crystal surface energy associated with the crystallization of acetyl salicylic acid from supersaturated aqueous/ethanol solution. *Cryst Growth Des*. 2006;6(6):1324–1334.
65. Kuznezov V. *Surface Energy of Solids*. London: H.M. Stationary Office; 1957.
66. Yusop SNA. *Characterisation of the Morphological and Surface Properties of Organic Micro-Crystalline Particles*. PhD Thesis. University of Leeds; 2014.
67. Hartman P, Bennema P. The attachment energy as a habit controlling factor: I. Theoretical considerations. *J Cryst Growth*. 1980;49(1):145–156.
68. Mayo SL, Olafson BD, Goddard WA. DREIDING: a generic force field for molecular simulations. *J Phys Chem*. 1990;94(26):8897–8909.
69. Wulff G. zur frage der geschwindigkeit des wachsthums und der auflösung der krystallflächen. *Z Kristallogr-Cryst Mater*. 1901;34(1−6):449–530.
70. Jaffari S, Forbes B, Collins E, Barlow DJ, Martin GP, Murnane D. Rapid characterisation of the inherent dispersibility of respirable powders using dry dispersion laser diffraction. *Int J Pharm*. 2013;447(1−2):124–131.
71. Dorris GM, Gray DG. Adsorption of n-alkanes at zero surface coverage on cellulose paper and wood fibers Author links open overlay panel. *J Colloid Interface Sci*. 1980;77(2):353–362.
72. Lavielle L, Schultz J. Surface properties of carbon fibers determined by inverse gas chromatography: role of pretreatment. *Langmuir*. 1991;7:978–981.
73. Bale H., Sun J., Gajjar P., et al. Laboratory diffraction contrast tomography (LabDCT): a new technique for measuring crystal habit and formulation structure. Respiratory Drug Delivery 2020 Digital. 2020.
74. Bachmann F, Bale H, Gueninchault N, Holzner C, Lauridsen EM. 3D grain reconstruction from laboratory diffraction contrast tomography. *J Appl Crystallogr*. 2019;52(3):643–651.
75. Inkscape Project. Inkscape, Available at: https://inkscape.org.; 2020.
76. Bryant MJ, Black SN, Blade H, Docherty R, Maloney AGP, Taylor SC. The CSD drug subset: the changing chemistry and crystallography of small molecule pharmaceuticals. *J Pharm Sci*. 2019;108(5):1655–1662. https://doi.org/10.1016/j.xphs.2018.12.011.
77. Lim S, Nickerson T. Effect of methanol on the various forms of lactose. *J Dairy Sci*. 1973;56(7):843–848.
78. Nickerson T, Lim S. Effect of various alcohols on lactose. *J Dairy Sci*. 1974;57(11):1320–1324.
79. Gillon AL, Feeder N, Davey RJ, Storey R. Hydration in molecular crystals - a cambridge structural database analysis. *Cryst Growth Des*. 2003;3(5):663–673.
80. Hebbink GA, Jaspers M, Peters HJW, Dickhoff BHJ. Recent developments in lactose blend formulations for carrier-based dry powder inhalation. *Adv Drug Deliv Rev*. 2022;189: 114527.
81. Sarangi S, Thalberg K, Frenning G. Effect of carrier size and mechanical properties on adhesive unit stability for inhalation: a numerical study. *Powder Technol*. 2021;390:230–239.
82. Hasrin NA, Irwan SN, Sapawe N, Ibrahim SF. Elucidating the intermolecular interactions and crystallographic structure of aspirin and lactose monohydrate by synthonic modelling. *Chem Eng Trans*. 2023;106:1081–1086.
83. Saxena A, Kendrick J, Grimsey IM, Roberts R, York P. A combined modelling and experimental study of the surface energetics of α-lactose monohydrate. *J Pharm Sci*. 2010;99(2):741–752. https://doi.org/10.1002/jps.21864.
84. Thielmann F, Burnett DJ, Heng JY. Determination of the surface energy distributions of different processed lactose. *Drug Dev Ind Pharm*. 2007;33(11):1240–1253.
85. Turner TD, Ma CY, Al Ayoub Y, et al. Calculating the surface energies of crystals on a face-specific and whole particle basis: case study of the α- and β-polymorphic forms of L-glutamic acid. *Powder Technol*. 2024;448: 120276.
86. Cline D, Dalby R. Predicting the quality of powders for inhalation from surface energy and area. *Pharm Res*. 2002;19(9):1274–1277. https://doi.org/10.1023/a:1020338405947.
87. Newell HE, Buckton G, Butler DA, Thielmann F, Williams DR. The use of inverse phase gas chromatography to measure the surface energy of crystalline, amorphous, and recently milled lactose. *Pharm Res*. 2001;18(5):662–666.
88. Ticehurst M, York P, Rowe R, Dwivedi S. Characterisation of the surface properties of α-lactose monohydrate with inverse gas chromatography, used to detect batch variation. *Int J Pharm*. 1996;141(1−2):93–99.
89. Raghavan S, Ristic R, Sheen D, Sherwood J, Trowbridge L, York P. Morphology of crystals of α-lactose hydrate grown from aqueous solution. *J Phys Chem B*. 2000;104(51):12256–12262.
90. Jones MD, Young P, Traini D. The use of inverse gas chromatography for the study of lactose and pharmaceutical materials used in dry powder inhalers. *Adv Drug Deliv Rev*. 2012;64(3):285–293.